Classification of solutions for guided waves in anisotropic composites with large numbers of layers

Armin M. A. Huber[1,a)] and Markus G. R. Sause[2]
[1]*Center for Lightweight Production Technology, Institute of Structures and Design, German Aerospace Center (DLR), Augsburg, Bavaria, 86159, Germany*
[2]*Mechanical Engineering, Institute of Materials Resource Management, University of Augsburg, Augsburg, Bavaria, 86159, Germany*

Guided waves are used for the non-destructive evaluation in automotive and aerospace industries. There is a trend leaning away from isotropic materials to the manufacturing based on composites. However, the elastic wave dynamics in such materials is considerably more complicated. Much effort has been committed to the calculation of guided waves' dispersion curves in composites. Lots of methods and tools are available, but it becomes difficult when there are more than one hundred layers. In this paper the calculation of dispersion diagrams and mode shapes using the stiffness matrix method is demonstrated. Boundary conditions are implemented into the stiffness matrix method that allow for the separate tracing of the various mode families. Shear horizontal modes are modeled with the transfer matrix method without facing any numerical instability. It is elucidated just how the occurrence of the mode families depends on the system's symmetry and wave propagation direction. As a result, the robustness and reliability of guided wave modeling by using the stiffness method is improved, and more information about the modes is yielded. This is demonstrated on exemplary layups of the fiber reinforced polymer T800/913, with up to 400 layers. Referencing is made against results from DISPERSE® (Imperial College London, London, UK) for selected cases.

I. INTRODUCTION

Guided waves have been used for non-destructive evaluation (NDE) for many decades. An early description of the flaw detection of sheets and tubes immersed in water by means of Rayleigh and Lamb waves was given by Viktorov already back in 1967.[1] Only a few years later, Luukkala *et al.* proposed a contactless test method for paper and metal plates based on Lamb waves.[2,3] Many applications have been established since then and the advent of composite materials in automotive and aerospace industries, which took place in the early 1990s, has added significant complexity to the non-destructive testing and evaluation processes. The ability of guided waves to propagate many meters in a waveguide is utilized for pipe inspection.[4,5] They are also used for the inspection of bonding,[6] which is one of the most challenging tasks, especially in the case of kissing bonds.[7] Other relevant studies concerning NDE and structural health monitoring (SHM) on composite structures are found in Refs. 8–15. The air-coupled version of the guided wave inspection could play an important role in future production lines. Often, the presence of a liquid coupling medium is unwanted because it might inflict damage to unsealed composite structures. Furthermore, the air-coupled version is more suitable for in-line non-destructive inspection (NDI), which improves the cost-efficiency of the manufacturing process. All of the following researchers have used the air-coupled variant. Castaings *et al.* have done significant work on the single-sided ultrasonic testing of composites by using Lamb waves,[16–19] while Solodov *et al.* have used them for transmissive inspection.[20–22] Mechanically induced fatigue on composites has been monitored by means of Lamb waves by Rheinfurth and Schmidt *et al.*[23,24] Holland and Chimenti have shown that the S_1 Lamb wave mode at zero group velocity allows for improved imaging capabilities,[25] and Raisutis *et al.* have investigated the inspection of composite rods used in aerospace.[26] The interaction of the A_0 Lamb wave mode with delaminations in composites has been studied both experimentally and by finite element modeling by Zenghua *et al.*[27]

The initial task for the work presented here was the calculation of incidence angles for the excitation of Lamb waves for the air-coupled ultrasonic testing of rocket booster pressure vessels of the future launcher Ariane 6. These vessels will be made of carbon fiber reinforced polymer (CFRP) in order to make them lighter and therefore enable the launcher to carry more payload. The ultrasonic incidence angle depends on the anisotropic laminate stiffness and its thickness. In some areas such pressure vessels can consist of up to 400 layers, depending on the manufacturing procedure (integral or differential) and the production technology (thermoplastic or wet winding or dry fiber layup followed by infusion), which is a challenging task to calculate them. To facilitate the calculation, it is a common practice to group layers, but this is not possible here because the layups are very complicated and irregular in terms of the winding angle

a)Electronic mail: armin.huber@dlr.de

(fiber direction) and layer thickness. Therefore, every single layer has to be calculated.

Since the early 1990s Lowe and Pavlakovic have developed the DISPERSE® software (Imperial College London, London, UK) for the guided wave modeling and analysis. Nowadays, due to its versatility and fast computing capabilities, DISPERSE® has become the leading software in its field. However, it is not suitable for the calculation of rocket booster laminates since currently it cannot calculate laminates containing more than 64 layers. Therefore, the stiffness matrix method has been implemented with MATLAB® R2015a (MathWorks, Natick, MA) for the calculation of Lamb and shear horizontal wave dispersion curves as well as the corresponding stress and displacement field components in CFRP-laminates. The code will be made available as freeware stand-alone software "Dispersion Calculator" on the German Aerospace Center (DLR) homepage.[28]

The stiffness matrix method is a reformulation of the transfer matrix method carried out by Rokhlin and Wang.[29,30] The transfer matrix method for a layered medium was developed by Thomson.[31] A small error in his work was corrected by Haskell,[32] and Nayfeh[33] extended the transfer matrix method to general anisotropic multilayered media. The transfer matrix method suffers from a numerical instability when the product of the layer thickness and frequency becomes large. Many attempts have been undertaken to overcome the problem, mostly with limited success and at the expense of the simple form of the original formulation. A different approach, which is used also by DISPERSE®, is the global matrix method proposed by Knopoff.[34] Here, a large single matrix comprises the equations of all layers. Schmidt and Tango[35] have shown that this method is numerically stable. However, the drawback of this method is that it might be slow when many layers have to be computed. Mal[36] extended the global matrix method to anisotropic multilayered media and Kausel and Roesset[37] conducted a reformulation for isotropic cases. The newer stiffness matrix method works numerically stable as well and is more efficient than the global matrix method when it comes to the calculation of many layers. At the same time, the concise form of the stiffness matrix method is easy to understand and code. The stiffness matrix method is used by many researchers, such as Kamal and Giurgiutiu[38] and most recently by Barski and Pajak.[39] An alternative to root-finding methods is the semi-analytical finite element (SAFE) method made popular by Gavric.[40] This method is more geometrically flexible than root-finding methods, where one is restricted to flat and cylindrical structures. The latest and possibly most powerful and versatile method is the spectral collocation method (SCM) developed by Quintanilla *et al.*[41] It is similar to SAFE in that it is using a one-dimensional mesh over the system thickness, but SCM possesses higher accuracy and speed of computation. Instead of solving a differential equation directly, the SCM method uses a spectral approximation that satisfies the differential equation and boundary conditions. The authors claim that SCM is easier to code than root-finding methods, it is faster, and most importantly, it can definitely not miss any mode solution. Only recently, the same authors have developed a classification of multilayered anisotropic waveguides according to their solution's properties.[42] All crystal classes and independent axes configurations can be assigned to one of only five different categories. A critical benefit is that modal solutions can be separated into mode families for which dispersion curves do not cross. This helps avoid the well-known jumping mode problem, which is present in root-finding methods in some situations. Furthermore, one can save time by computing only a single mode family if one is not interested in the other ones.

The aim of the present paper is to apply such a classification with the stiffness matrix method. This is achieved by the implementation of appropriate boundary conditions. In particular, it will be focused on the determination of symmetric and antisymmetric Lamb and shear horizontal waves as well as the calculation of internal stress and displacement field components. The transfer matrix is used for shear horizontal waves without facing the numerical instability. The different situations encountered in symmetric and nonsymmetric layups, as well as the coupling and decoupling of solutions, are addressed. To demonstrate the capabilities of our approach on laminates with large numbers of layers, we present the calculation of a laminate consisting of 400 layers.

The paper is organized as follows. In Sec. II, the transfer matrix is introduced, first for the general case and then for wave propagation along axes of symmetry where Lamb and shear horizontal waves decouple. Based on Nayfeh's formalism for shear horizontal waves, shown in Ref. 33, we introduce case-dependent adaptations on the transfer matrix and the characteristic equations for the determination of modal solutions. Here, we did not encounter any numerical instability. Then we present a formalism for the calculation of the stress and displacement field components of shear horizontal waves. Section III covers the stiffness matrix method for the general and decoupled cases. We propose an alternative form of the global stiffness matrix for symmetric layups with a different symmetry identity matrix as the one presented by Rokhlin and Wang in Refs. 29 and 30. For the calculation of the stress and displacement field components in multilayered systems, we use Rokhlin and Wang's "backpropagation" recursive algorithm, but we suggest a more concise equation for the determination of the reflected and transmitted wave amplitudes. We present also a simple equation for the calculation of the stress and displacement field components in a single-layered plate. Then we carry out the abovementioned algorithms for Lamb waves in the decoupled case. In Sec. IV, the dispersion curve tracing routines used by the MATLAB®-based Dispersion Calculator are explained, and the used boundary conditions are summarized to give the reader a fast overview and help him with his own implementation. Numerical dispersion curve simulations in exemplary layups consisting of the CFRP T800/913 are presented in Sec. V. Some displacement and stress fields that visualize the differences between the mode families are plotted and discussed.

II. THE TRANSFER MATRIX METHOD

In this section, the global transfer matrix is formulated for the general case, i.e., when the composite contains layers

with arbitrary azimuthal fiber orientations and arbitrary wave propagation directions within the main plane of the plate. Then the solutions for pure shear horizontally polarized waves in the special case of wave propagation along axes of symmetry are presented. These solutions have been used for the numerical examples shown in Sec. V since they do not suffer from the same numerical instability as the general solutions and as those for pure Lamb wave modes in the decoupled case do.

A. General layered composite

The dynamic behavior of a linear elastic, generally anisotropic solid is given by the tensorial equations of motion, written in the crystallographic coordinate system $x'_i = (x'_1, x'_2, x'_3)$, as

$$\frac{\partial \sigma'_{ij}}{\partial x'_j} = \rho \frac{\partial^2 u'_i}{\partial t^2} \tag{1}$$

and the general tensorial stress-strain relation as

$$\sigma'_{ij} = c'_{ijkl}\varepsilon'_{kl}, \quad i,j,k,l = 1,2,3, \tag{2}$$

where σ'_{ij} and ε'_{kl} are the stress and strain tensors, respectively, u'_i is the displacement vector and ρ the material density. c'_{ijkl} is the stiffness tensor containing the elastic material constants. In this paper the calculations are carried out on plates consisting of unidirectional layers of the fiber reinforced polymer T800/913. This material has transversely isotropic symmetry. Therefore, according to Ref. 43, Eq. (2) is given as

$$\begin{bmatrix} \sigma'_{11} \\ \sigma'_{22} \\ \sigma'_{33} \\ \sigma'_{23} \\ \sigma'_{13} \\ \sigma'_{12} \end{bmatrix} = \begin{bmatrix} C'_{11} & C'_{12} & C'_{12} & 0 & 0 & 0 \\ & C'_{22} & C'_{23} & 0 & 0 & 0 \\ & & C'_{22} & 0 & 0 & 0 \\ & & & \frac{1}{2}(C'_{22}-C'_{23}) & 0 & 0 \\ & & \text{sym} & & C'_{55} & 0 \\ & & & & & C'_{55} \end{bmatrix} \times \begin{bmatrix} \varepsilon'_{11} \\ \varepsilon'_{22} \\ \varepsilon'_{33} \\ \gamma'_{23} \\ \gamma'_{13} \\ \gamma'_{12} \end{bmatrix}, \tag{3}$$

wherein the expanded matrix form of the stiffness tensor is used and $\gamma'_{kl} = 2\varepsilon'_{kl}$. By using uppercase C's, the expanded matrix form is distinguished from the lowercase c's of the contracted tensor form. Since layers with different fiber orientation angles Φ within the x_1–x_2-plane are stacked onto each other, it is convenient to transform the stiffness matrix into a global coordinate system $x_i = (x_1, x_2, x_3)$ for each layer. Each layer's local coordinate system x'_i is rotated about the x_3-direction by an angle Φ so that x'_3 and x_3 coincide and their origins reside on the top of the respective layer. Hence, the transformation operations for orthotropic systems[33] (including transversely isotropic ones), given in Appendix A, are performed upon the stiffness matrix, yielding the transformed stiffness matrix components.

Consider a plate consisting of an arbitrary number of layers N rigidly bonded at their interfaces and surrounded by a vacuum that is situated in the global coordinate system such that the incident plane coincides with the x_1–x_3-plane (see Fig. 1). Guided wave propagation is restricted to be along the x_1-direction ($\Theta = 90°$). The fundamental physical concept behind the behavior of guided waves is based on the propagation and superposition of partial waves. When an incident wave hits the top interface of the first (uppermost) layer, a certain number of reflected and transmitted partial waves will be generated. The transmitting ones are refracted according to Snell's law. These are three partial waves propagating downward (along the $-x_3$-direction) and another three being reflected from the bottom interface of the first layer and propagating upward (along the $+x_3$-direction). Again, at the bottom of the first layer, a certain proportion of energy is transmitted into the second layer while the rest gets reflected. Hence, six partial waves are propagating in each layer, namely two longitudinally polarized ones (L^-, L^+), two shear vertically polarized ones (SV^-, SV^+, with particle displacement in the x_1–x_3-plane) and two shear horizontally polarized ones (SH^-, SH^+, with particle displacement along x_2). If all partial waves, as well as the incident wave, share the same projected wavenumber k along the x_1-direction on each interface, a propagating guided wave is generated by the superposition of the partial waves. Therefore, it is of fundamental importance to find the propagation directions of all partial waves in each layer. According to Ref. 45, this is achieved by solving the Christoffel equation

$$\rho \frac{\partial^2 u_i}{\partial t^2} = c_{ijkl} \frac{\partial^2 u_l}{\partial x_j \partial x_k}, \tag{4}$$

which has the general form of solution for the displacement field components u_i in terms of the partial wave amplitudes U_i, $i = 1,2,3$,

$$(u_1, u_2, u_3) = (U_1, U_2, U_3)\mathrm{e}^{\mathrm{i}k(x_1 \sin\Theta + \alpha x_3 - vt)}, \tag{5}$$

where k is the x_1-component of the wavenumber, v is the phase velocity ($=\omega/k$) along x_1, ω is the angular frequency, t is the time, and α is an unknown ratio of the wavenumber components along the x_3- and x_1-directions.

By substituting Eq. (5) into the expanded displacement field equations obtained from Eq. (4), which are skipped here for brevity (these equations are given in Refs. 33 and 39), three coupled equations are obtained,

$$\begin{bmatrix} C_{11}-\rho v^2+C_{55}\alpha^2 & C_{16}+C_{45}\alpha^2 & (C_{13}+C_{55})\alpha \\ & C_{66}-\rho v^2+C_{44}\alpha^2 & (C_{36}+C_{45})\alpha \\ \text{sym} & & C_{55}-\rho v^2+C_{33}\alpha^2 \end{bmatrix} \times \begin{bmatrix} U_1 \\ U_2 \\ U_3 \end{bmatrix} = 0. \tag{6}$$

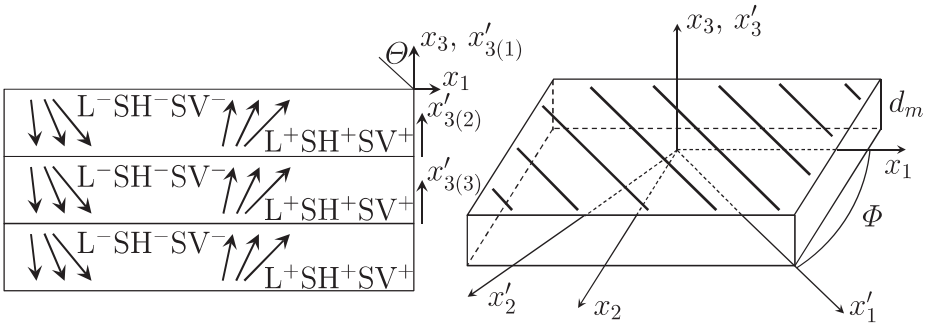

FIG. 1. Layered plate (left) and single layer (right) with local and global coordinate systems (Refs. 33 and 44).

Nontrivial solutions for U_1,U_2,U_3 require the vanishing of the determinant of the 3×3 matrix in Eq. (6) and yield the sixth-degree polynomial equation

$$\alpha^6 + A_1\alpha^4 + A_2\alpha^2 + A_3 = 0. \tag{7}$$

A revision of the coefficients A_2 and A_3 as published in Ref. 33 is presented in Appendix B, since several exponents were missing by accident. Equation (7) has six solutions for α, where

$$\alpha_2 = -\alpha_1, \quad \alpha_4 = -\alpha_3, \quad \alpha_6 = -\alpha_5. \tag{8}$$

Substituting α_q, $q=1,2,\ldots6$, into Eq. (6) delivers the partial wave amplitude ratios $V_q = U_{2q}/U_{1q}$ and $W_q = U_{3q}/U_{1q}$, namely,

$$V_q = \frac{K_{11}(\alpha_q)K_{23}(\alpha_q) - K_{13}(\alpha_q)K_{12}(\alpha_q)}{K_{13}(\alpha_q)K_{22}(\alpha_q) - K_{12}(\alpha_q)K_{23}(\alpha_q)}, \tag{9}$$

$$W_q = \frac{K_{11}(\alpha_q)K_{22}(\alpha_q) - K_{12}(\alpha_q)^2}{K_{12}(\alpha_q)K_{23}(\alpha_q) - K_{22}(\alpha_q)K_{13}(\alpha_q)}, \tag{10}$$

where the elements $K_{ij}(\alpha_q)$, $i,j=1,2,3$, are the components of the 3×3 matrix in Eq. (6). Now, for convenience, the new variable $\sigma^*_{ij} = \sigma_{ij}/\mathrm{i}k$ is introduced. Thus, the displacement and stress field components can be written as

$$(u_1,u_2,u_3) = \sum_{q=1}^{6}(1,V_q,W_q)U_{1q}\mathrm{e}^{\mathrm{i}k(x_1\sin\Theta+\alpha x'_3-vt)}, \tag{11}$$

$$(\sigma^*_{33},\sigma^*_{13},\sigma^*_{23}) = \sum_{q=1}^{6}(D_{1q},D_{2q},D_{3q})U_{1q}\mathrm{e}^{\mathrm{i}k(x_1\sin\Theta+\alpha x'_3-vt)}, \tag{12}$$

where

$$\begin{aligned} D_{1q} &= C_{13} + C_{36}V_q + C_{33}\alpha_q W_q,\\ D_{2q} &= C_{55}(\alpha_q + W_q) + C_{45}\alpha_q V_q,\\ D_{3q} &= C_{45}(\alpha_q + W_q) + C_{44}\alpha_q V_q. \end{aligned} \tag{13}$$

Now, Eqs. (11) and (12) can be combined and written in expanded matrix form as given in Appendix C. Equation (C1) relates the displacement and stress field components at the top of the mth layer ($x'_{3(m)} = 0$) to those at its bottom ($x'_{3(m)} = -d_m$), where d_m is the thickness of the mth layer. To facilitate the further discussion, the first 6×6 matrix in Eq. (C1) is designated as $\mathbf{X}_m$ and the diagonal matrix as $\mathbf{E}_m$. The local transfer matrix $\mathbf{A}_m$ for the layer m is then given by

$$\mathbf{A}_m = \mathbf{X}_m\mathbf{E}_m\mathbf{X}_m^{-1}, \tag{14}$$

and the global transfer matrix $\mathbf{A}$ is obtained by the multiplication of the individual local transfer matrices

$$\mathbf{A} = \mathbf{A}_m\mathbf{A}_{m-1}\cdots\mathbf{A}_1. \tag{15}$$

The global transfer matrix can be used to relate the displacements and stresses at the top to those at the bottom of the whole plate

$$\mathbf{S}_{-d} = \mathbf{A}\mathbf{S}_0. \tag{16}$$

Here, $\mathbf{S}_{-d}$ is the 6×1 displacement and stress matrix at the bottom surface of the plate ($x_3 = -d$) and $\mathbf{S}_0$ that one at the top surface of the plate ($x_3 = 0$), where d is the thickness of the plate. To find modal solutions of Eq. (16), the stress free upper and lower surface is invoked,

$$\sigma^*_{i3} = 0, \quad i = 1,2,3. \tag{17}$$

This means that no energy is leaking to the surrounding medium, as is the case in a vacuum. Using the acoustical impedances $Z=\rho v$ of aluminum ($\rho = 2700\,\mathrm{kg/m^3}$, $v = 6320\,\mathrm{m/s}$), air ($\rho = 1.2\,\mathrm{kg/m^3}$, $v = 343\,\mathrm{m/s}$), and water ($\rho = 1000\,\mathrm{kg/m^3}$, $v = 1500\,\mathrm{m/s}$), and calculating the transmission $T = 2Z_1/(Z_1+Z_2)$ through the respective interface delivers values of $T_{\mathrm{alu/air}} = 4.8\times10^{-5}$ and $T_{\mathrm{alu/water}} = 0.16$. This demonstrates that assuming a vacuum ($T_{\mathrm{alu/vacuum}} = 0$) is a good approximation for air as surrounding medium but not for water. Now, Eq. (16) may be written in the form

$$\begin{bmatrix} u_1\\ u_2\\ u_3\\ 0\\ 0\\ 0 \end{bmatrix}_{-d} = \mathbf{A}\begin{bmatrix} u_1\\ u_2\\ u_3\\ 0\\ 0\\ 0 \end{bmatrix}_0 \quad\rightarrow\quad \begin{bmatrix} 0\\ 0\\ 0 \end{bmatrix} = \begin{bmatrix} a_{41} & a_{42} & a_{43}\\ a_{51} & a_{52} & a_{53}\\ a_{61} & a_{62} & a_{63} \end{bmatrix}\begin{bmatrix} u_1\\ u_2\\ u_3 \end{bmatrix}_0, \tag{18}$$

which requires the 3×3 submatrix to be singular. Therefore, the characteristic function for the system is

$$\det\begin{bmatrix} a_{41} & a_{42} & a_{43} \\ a_{51} & a_{52} & a_{53} \\ a_{61} & a_{62} & a_{63} \end{bmatrix} = 0. \tag{19}$$

Equation (19) can be solved numerically in order to determine the guided wave's phase velocity dispersion versus frequency or wavenumber.

B. Propagation along axes of symmetry

The physical reason why we do not encounter the numerical instability in the following algorithms is because the partial waves in shear horizontal waves are never evanescent. According to Ref. 29, the mathematical reason for the numerical instability for layer thicknesses of several wavelengths is because the inverse matrix of a singular matrix, as it is required in Eq. (14), does not exist. As will be shown below, this matrix inversion is not part of the numerical computation process if one solves for the shear horizontally polarized modes in the case of wave propagation along axes of symmetry. Then the solutions decouple into pure Lamb and shear horizontal modes, but this is possible only in layups that contain solely layers with fiber orientations along the 0° and 90° directions, while the wave propagation must be along either of those directions as well (see Fig. 2). Hence, x_3 coincides with x'_3 and x_1 can coincide with either x'_1 or x'_2 for 0° or 90° orientation, respectively. The propagation of shear horizontal waves is the simplest case in anisotropic media, since only one displacement field component is involved. Therefore, according to Ref. 33, the equation of motion is relatively simple, namely,

$$C'_{66}\frac{\partial^2 u'_2}{\partial x'^2_1} + C'_{44}\frac{\partial^2 u'_2}{\partial x'^2_3} = \rho\frac{\partial^2 u'_2}{\partial t^2}, \tag{20}$$

and the corresponding stress-strain relation

$$\sigma'_{23} = C'_{44}\frac{\partial u'_2}{\partial x'_3}. \tag{21}$$

The formal solutions of Eqs. (20) and (21) under consideration of $\Theta = 90°$ are

$$u_2 = \sum_{q=1}^{2} U_{2q} e^{ik(x_1+\alpha x'_3 - vt)} \tag{22}$$

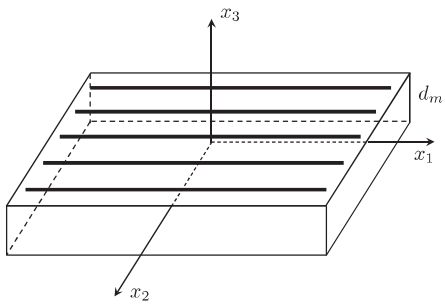

FIG. 2. Anisotropic plate showing wave propagation along an axis of symmetry (Ref. 33).

$$\sigma^*_{23} = \sum_{q=1}^{2} D_{2q} U_{2q} e^{ik(x_1+\alpha x'_3 - vt)}, \tag{23}$$

respectively, where

$$D_{2q} = C_{44}\alpha_q, \quad \alpha_{1,2} = \pm\sqrt{\frac{\rho v^2 - C_{66}}{C_{44}}}. \tag{24}$$

By using superposition, the displacement and stress field components can be given by

$$\begin{bmatrix} u_2 \\ \sigma^*_{23} \end{bmatrix} = \begin{bmatrix} 1 & 1 \\ C_{44}\alpha_1 & -C_{44}\alpha_1 \end{bmatrix} \begin{bmatrix} U_{21} e^{ik(x_1+x'_3\alpha_1 - vt)} \\ U_{22} e^{-ik(x_1+x'_3\alpha_1 - vt)} \end{bmatrix}, \tag{25}$$

and with the use of Eq. (14) one can manipulate Eq. (25) into

$$\begin{bmatrix} u_2 \\ \sigma^*_{23} \end{bmatrix}_{x'_{3m}=-d_m} = \begin{bmatrix} \cos\gamma_m & i\sin\gamma_m/D_m \\ iD_m\sin\gamma_m & \cos\gamma_m \end{bmatrix} \begin{bmatrix} u_2 \\ \sigma^*_{23} \end{bmatrix}_{x'_{3m}=0}, \tag{26}$$

where $\gamma_m = \alpha_m k d_m$ and $D_m = \alpha_m C_{44}$. With the 2×2 matrix in Eq. (26), one has obtained an analytical expression for the individual local transfer matrix $\mathbf{A}_m$ that contains the matrix inversion *a priori*, which means that it does not have to be performed in the numerical computation procedure where it can cause the instability.

Similar to what has been shown in Sec. II A, Eq. (26) relates the displacement and stress field components at the top of the mth layer ($x'_{3(m)} = 0$) to those at its bottom ($x'_{3(m)} = -d_m$). Finally, the global transfer matrix $\mathbf{A}$ is again achieved by the multiplication of the individual local transfer matrices according to Eq. (15),

$$\begin{bmatrix} u_2 \\ \sigma^*_{23} \end{bmatrix}_{x_3=-d} = \begin{bmatrix} a_{11} & a_{12} \\ a_{21} & a_{22} \end{bmatrix} \begin{bmatrix} u_2 \\ \sigma^*_{23} \end{bmatrix}_{x_3=0}, \tag{27}$$

relating the displacement and stress at the bottom surface of the plate ($x_3 = -d$) to that one at the top surface of the plate ($x_3 = 0$). Modal solutions are determined by imposing stress free plate surfaces, which leads to the simple characteristic function

$$a_{21} = 0. \tag{28}$$

If the plate consists of an n-times repetition of a unit cell, the condition

$$\begin{bmatrix} u_2 \\ \sigma^*_{23} \end{bmatrix}_{x_3=-d} = \begin{bmatrix} u_2 \\ \sigma^*_{23} \end{bmatrix}_{x_3=0} e^{ikd\cos\Theta} \tag{29}$$

must be satisfied. Then, with $\Theta = 90°$, the characteristic function for modal solutions is

$$\det\begin{bmatrix} a_{11}-1 & a_{12} \\ a_{21} & a_{22}-1 \end{bmatrix} = 0. \tag{30}$$

Note that the fundamental shear horizontal mode is nondispersive in the decoupled case with $v = \sqrt{C_{66}/\rho}$.

Since the expressions shown in Sec. II B are not susceptible to the numerical instability, they have been used for the calculation of the numerical examples, except in one instance, where a routine based on the stiffness matrix method has been used instead.

Based on the above formalism for shear horizontal modes, in Secs. II B 1 and II B 2 we present adaptations on Eqs. (26), (28), and (30) since the modal solutions could not have been obtained successfully with them for every layup type and mode shape symmetry. In Sec. II B 3, we introduce our calculation routine for the internal stress and displacement fields in shear horizontal modes. The displacement field is necessary to identify, if it exists, the symmetric or antisymmetric character of the modes.

The following discussion is conducted for symmetric and non-symmetric layups separately. The reason for this is that guided waves, be it Lamb- or shear horizontal modes, have a definite symmetric or antisymmetric character in terms of the displacement field component u_1 for Lamb modes and u_2 for shear horizontal mods only in symmetric layups. This can be a single layer or a layup that is mirrored in terms of its fiber orientation, as well as the layer thickness with respect to the middle plane of the plate. Then $u_{1/2}$ have the same absolute value and polarity at the top and bottom surface of the plate in such cases of symmetric modes, and the same absolute value but opposite polarity at the extreme surfaces in cases of antisymmetric modes.

In the following, the local transfer matrix contained in Eq. (26) is denoted as $\mathbf{A}_m^c$, where the c-index indicates that the matrix contains complex values. A second matrix $\mathbf{A}_m^r$ is introduced that is actually $\mathbf{A}_m^c$, but without the two imaginary numbers "i" in it. This matrix contains only real numbers

$$\mathbf{A}_m^r = \begin{bmatrix} \cos\gamma_m & \sin\gamma_m/D_m \\ D_m \sin\gamma_m & \cos\gamma_m \end{bmatrix}. \tag{31}$$

1. Symmetric layups

For a single layer, the characteristic function for symmetric and antisymmetric shear horizontal modes is

$$a_{21(m)}^r = 0, \quad m = 1. \tag{32}$$

If one considers a multilayered, symmetric layup, and solves for the symmetric modes, then one has to distinguish two cases. If it contains only one unit cell that is mirrored, like $[0/90]_s$, then one has to multiply the local transfer matrices according to

$$\mathbf{A}^r = \mathbf{A}_4^r \mathbf{A}_3^r \mathbf{A}_2^r \mathbf{A}_1^r, \tag{33}$$

and then solve

$$a_{21}^r = \min. \tag{34}$$

Here, "min" means that minima have to be found since the function does not, or only in some instances, cross zero. In contrast, if the layup contains more than one mirrored unit cell, i.e., it is a periodic structure, e.g., $[0/90]_{ns}$, $n = 2,3,\ldots$, one has to multiply the complex local transfer matrices according to

$$\mathbf{A}^c = \mathbf{A}_m^c \mathbf{A}_{m-1}^c \cdots \mathbf{A}_1^c, \tag{35}$$

and solve after the symmetric modes by using

$$\det \begin{bmatrix} a_{11}^c - 1 & a_{12}^c \\ a_{21}^c & a_{22}^c - 1 \end{bmatrix} = \min. \tag{36}$$

Antisymmetric modes in layups that contain more than one layer could not have been solved successfully in transfer matrix style. The solution of these is presented in Sec. III B 2.

2. Non-symmetric layups

As stated above, no separation into symmetric and antisymmetric modes is possible in non-symmetric layups. The simplest layup possible is [0/90]. This has to be processed by the usual multiplication operation

$$\mathbf{A}^r = \mathbf{A}_2^r \mathbf{A}_1^r, \tag{37}$$

followed by

$$a_{21}^r = 0. \tag{38}$$

In case of multiple repetitions, like $[0/90]_n$, $n = 2,3,\ldots$, the solution depends on the order p of the respective mode. The fundamental shear horizontal mode (which is non-dispersive) has the order $p = 0$. The higher order modes are counted in the sequence of increasing critical frequency/wavenumber by $p = 1,2,\ldots$, i.e., from left to right in the dispersion diagram. If the mode order is an integer multiple of the number of repetitions n, i.e., $p/n = 1,2,\ldots$, one has to use

$$\mathbf{A}^r = \mathbf{A}_m^r \mathbf{A}_{m-1}^r \cdots \mathbf{A}_1^r \tag{39}$$

and solve Eq. (38). Otherwise one needs Eq. (35), and then solve

$$\det \begin{bmatrix} a_{11}^c - 1 & a_{12}^c \\ a_{21}^c & a_{22}^c + 1 \end{bmatrix} = 0. \tag{40}$$

Notice the different sign in Eq. (40) as compared to Eq. (36).

3. Displacement and stress field component calculation

In the following, it is important to return the imaginary identity to the local transfer matrices $\mathbf{A}_m^r$ with only real numbers in it. That is achieved by the element-wise multiplication

$$\mathbf{A}_m^c = \mathbf{A}_m^r \circ \begin{bmatrix} 1 & \mathrm{i} \\ \mathrm{i} & 1 \end{bmatrix}. \tag{41}$$

An m-layered plate has $m+1$ interfaces, where $m = 1$ corresponds to the top surface and $m+1$ corresponds to the bottom surface. First, one has to calculate the displacement and

stress field components $u_{2(m)}$ and $\sigma^*_{23(m)}$ at all interfaces, assuming their continuity at the interfaces. One starts with the uppermost layer $m=1$. At the top of this layer the displacement is set to $u_{2(1)}=1$ and the stress to $\sigma^*_{23(1)}=0$. Then $u_{2(2)}$ and $\sigma^*_{23(2)}$ at the bottom of this layer can be obtained via its local transfer matrix

$$\begin{bmatrix} u_2 \\ \sigma^*_{23} \end{bmatrix}_2 = \begin{bmatrix} a^c_{11(1)} & a^c_{12(1)} \\ a^c_{21(1)} & a^c_{22(1)} \end{bmatrix} \begin{bmatrix} u_2 \\ \sigma^*_{23} \end{bmatrix}_1, \tag{42}$$

which results in

$$u_{2(2)} = a^c_{11(1)}, \quad \sigma^*_{23(2)} = a^c_{21(1)}. \tag{43}$$

To get $u_{2(3)}$ and $\sigma^*_{23(3)}$ at the bottom of the second layer ($m=2$), one must multiply the local transfer matrices of the first and second layers

$$\mathbf{A}^{*c} = \mathbf{A}^c_{(1)}\mathbf{A}^c_{(2)}. \tag{44}$$

Here, $\mathbf{A}^{*c}$ is the transfer matrix relating the displacement and stress field components at the top of the uppermost layer (i.e., at the top of the plate), to those at the bottom of the second layer. Substituting $\mathbf{A}^{*c}$ into Eq. (42) and considering the stress free upper plate surface yields

$$u_{2(3)} = a^{*c}_{11}, \quad \sigma^*_{23(3)} = a^{*c}_{21}. \tag{45}$$

This procedure has to be repeated until one has obtained the displacement $u_{2(m+1)}$ and stress $\sigma^*_{23(m+1)}$ at the bottom of the plate. Once the displacements and stresses are obtained at all interfaces, it is possible to calculate both components inside each layer. The now known displacements $u^0_{2(m)}$ and stresses $\sigma^{*0}_{23(m)}$ at the top ($x'_{3(m)}=0$) and bottom $u^{-d}_{2(m)}$, $\sigma^{*-d}_{23(m)}$, ($x'_{3(m)}=-d_m$) interface of the mth layer can be written in terms of their respective local transfer matrix and partial wave amplitudes

$$u^0_{2(m)} = a^c_{11(m)}U_{21(m)} + a^c_{12(m)}U_{22(m)}\mathrm{e}^{\mathrm{i}k\alpha_m d_m}, \tag{46}$$

$$u^{-d}_{2(m)} = a^c_{11(m)}U_{21(m)}\mathrm{e}^{\mathrm{i}k\alpha_m d_m} + a^c_{12(m)}U_{22(m)}, \tag{47}$$

$$\sigma^{*0}_{23(m)} = a^c_{21(m)}U_{21(m)} + a^c_{22(m)}U_{22(m)}\mathrm{e}^{\mathrm{i}k\alpha_m d_m}, \tag{48}$$

$$\sigma^{*-d}_{23(m)} = a^c_{21(m)}U_{21(m)}\mathrm{e}^{\mathrm{i}k\alpha_m d_m} + a^c_{22(m)}U_{22(m)}. \tag{49}$$

Here, the common factor $\mathrm{e}^{\mathrm{i}k(x_1-vt)}$ is suppressed since only the x_3-dependency of the displacement and stress is of interest. From Eqs. (46) to (49), the partial wave amplitudes are deduced as follows:

$$U^u_{21(m)} = \frac{u^0_{2(m)} - \dfrac{u^0_{2(m)}\mathrm{e}^{\mathrm{i}k\alpha_m d_m} - u^{-d}_{2(m)}}{\mathrm{e}^{2\mathrm{i}k\alpha_m d_m}-1}\mathrm{e}^{\mathrm{i}k\alpha_m d_m}}{a^c_{11(m)}}, \tag{50}$$

$$U^u_{22(m)} = \frac{u^0_{2(m)}\mathrm{e}^{\mathrm{i}k\alpha_m d_m} - u^{-d}_{2(m)}}{a^c_{12(m)}\left(\mathrm{e}^{2\mathrm{i}k\alpha_m d_m}-1\right)}, \tag{51}$$

$$U^\sigma_{21(m)} = \frac{\sigma^{*0}_{23(m)} - \dfrac{\sigma^{*0}_{23(m)}\mathrm{e}^{\mathrm{i}k\alpha_m d_m} - \sigma^{*-d}_{23(m)}}{\mathrm{e}^{2\mathrm{i}k\alpha_m d_m}-1}\mathrm{e}^{\mathrm{i}k\alpha_m d_m}}{a^c_{21(m)}}, \tag{52}$$

$$U^\sigma_{22(m)} = \frac{\sigma^{*0}_{23(m)}\mathrm{e}^{\mathrm{i}k\alpha_m d_m} - \sigma^{*-d}_{23(m)}}{a^c_{22(m)}\left(\mathrm{e}^{2\mathrm{i}k\alpha_m d_m}-1\right)}. \tag{53}$$

Now the displacement and stress at any point x'_3 inside the mth layer can be calculated by using

$$u_{2(m)} = a^c_{11(m)}U^u_{21(m)}\mathrm{e}^{\mathrm{i}k\alpha_m x'_3} + a^c_{12(m)}U^u_{22(m)}\mathrm{e}^{\mathrm{i}k\alpha_m (d_m - x'_3)}, \tag{54}$$

$$\sigma^*_{23(m)} = a^c_{21(m)}U^\sigma_{21(m)}\mathrm{e}^{\mathrm{i}k\alpha_m x'_3} + a^c_{22(m)}U^\sigma_{22(m)}\mathrm{e}^{\mathrm{i}k\alpha_m (d_m - x'_3)}. \tag{55}$$

This procedure can be done for every layer in order to obtain the complete displacement and stress field profile of a layup.

If symmetric and antisymmetric shear horizontal modes exist, it is possible to determine their character very fast. Just set the displacement at the top of the plate to $u^0_2 = 1$. Then the displacement at the bottom of the plate is given by $u^{-d}_2 = a^c_{11}$, where $\mathbf{A}^c$ is the global transfer matrix. If u^{-d}_2 is positive the shear horizontal mode is symmetric, and if u^{-d}_2 is negative the shear horizontal mode is antisymmetric.

III. THE STIFFNESS MATRIX METHOD

Similarly, as in Sec. II, the stiffness matrix is first introduced for the general case and then it is specialized to the case when the decoupling of Lamb and shear horizontal modes occurs. The calculation of the displacement and stress field components is presented for both cases.

A. General layered composite

Rokhlin and Wang[29] have rearranged the transfer matrix formulation into a numerically stable form, which is called the stiffness matrix $\mathbf{K}$. In contrast to the transfer matrix, the stiffness matrix relates the stresses at the top $\boldsymbol{\sigma}^*_m$ and bottom $\boldsymbol{\sigma}^*_{m+1}$ of the mth layer to the displacements at the top $\mathbf{u}_m$ and the bottom $\mathbf{u}_{m+1}$,

$$\begin{bmatrix} \boldsymbol{\sigma}^*_m \\ \boldsymbol{\sigma}^*_{m+1} \end{bmatrix} = \begin{bmatrix} \mathbf{D}^- & \mathbf{D}^+\mathbf{H} \\ \mathbf{D}^-\mathbf{H} & \mathbf{D}^+ \end{bmatrix}_m \begin{bmatrix} \mathbf{P}^- & \mathbf{P}^+\mathbf{H} \\ \mathbf{P}^-\mathbf{H} & \mathbf{P}^+ \end{bmatrix}^{-1}_m \begin{bmatrix} \mathbf{u}_m \\ \mathbf{u}_{m+1} \end{bmatrix} = \mathbf{K}_m \begin{bmatrix} \mathbf{u}_m \\ \mathbf{u}_{m+1} \end{bmatrix}. \tag{56}$$

Kamal and Giurgiutiu[38] have presented Eq. (56) in a form that is well suited for its implementation into code and which is reproduced in Appendix D 1. In order to obtain the global stiffness matrix of a multilayered plate, the local layer stiffness matrices $\mathbf{K}_m$ must be calculated first. Consider the local stiffness matrices of two neighboring layers

$$\begin{bmatrix}\boldsymbol{\sigma}_1^*\\ \boldsymbol{\sigma}_2^*\end{bmatrix}=\begin{bmatrix}\mathbf{K}_{11}^A & \mathbf{K}_{12}^A\\ \mathbf{K}_{21}^A & \mathbf{K}_{22}^A\end{bmatrix}\begin{bmatrix}\mathbf{u}_1\\ \mathbf{u}_2\end{bmatrix},\quad \begin{bmatrix}\boldsymbol{\sigma}_2^*\\ \boldsymbol{\sigma}_3^*\end{bmatrix}=\begin{bmatrix}\mathbf{K}_{11}^B & \mathbf{K}_{12}^B\\ \mathbf{K}_{21}^B & \mathbf{K}_{22}^B\end{bmatrix}\begin{bmatrix}\mathbf{u}_2\\ \mathbf{u}_3\end{bmatrix}. \tag{57}$$

Then Rokhlin and Wang's recursive algorithm is used to combine them

$$\begin{bmatrix}\boldsymbol{\sigma}_1^*\\ \boldsymbol{\sigma}_3^*\end{bmatrix}=\begin{bmatrix}\mathbf{K}_{11}^A+\mathbf{K}_{12}^A(\mathbf{K}_{11}^B-\mathbf{K}_{22}^A)^{-1}\mathbf{K}_{21}^A & -\mathbf{K}_{12}^A(\mathbf{K}_{11}^B-\mathbf{K}_{22}^A)^{-1}\mathbf{K}_{12}^B\\ \mathbf{K}_{21}^B(\mathbf{K}_{11}^B-\mathbf{K}_{22}^A)^{-1}\mathbf{K}_{21}^A & \mathbf{K}_{22}^B-\mathbf{K}_{21}^B(\mathbf{K}_{11}^B-\mathbf{K}_{22}^A)^{-1}\mathbf{K}_{12}^B\end{bmatrix}\begin{bmatrix}\mathbf{u}_1\\ \mathbf{u}_3\end{bmatrix}. \tag{58}$$

Calling the obtained matrix $\mathbf{K}^A$ and the stiffness matrix of the third layer $\mathbf{K}^B$, one can recursively use Eq. (58) to obtain the global stiffness matrix, which relates the stresses and displacements at the top and the bottom of the whole plate. If the plate consists of a periodic repetition of a unit cell, one can denote the stiffness matrix of the unit cell $\mathbf{K}^A$ and use Eq. (58) with $\mathbf{K}^B=\mathbf{K}^A$ as many times as repetitions are contained in the plate. By that way, the global stiffness matrix can be obtained very efficiently without recursively multiplying every single local stiffness matrix in every repetition. If the layup is symmetric, one has to calculate the stiffness matrix of one half of the layup $\mathbf{K}^A$. Our alternative formalism to the one presented by Rokhlin and Wang for the global stiffness matrix $\mathbf{K}$ is given by

$$\begin{bmatrix}\boldsymbol{\sigma}_1^*\\ \boldsymbol{\sigma}_3^*\end{bmatrix}=\begin{bmatrix}\mathbf{K}_{11}^A+\mathbf{K}_{12}^A(\mathbf{K}_{22}^A\circ\mathbf{I}-\mathbf{K}_{22}^A)^{-1}\mathbf{K}_{21}^A & -\mathbf{K}_{12}^A(\mathbf{K}_{22}^A\circ\mathbf{I}-\mathbf{K}_{22}^A)^{-1}(\mathbf{K}_{21}^A\circ\mathbf{I})\\ (\mathbf{K}_{12}^A\circ\mathbf{I})(\mathbf{K}_{22}^A\circ\mathbf{I}-\mathbf{K}_{22}^A)^{-1}\mathbf{K}_{21}^A & \mathbf{K}_{11}^A\circ\mathbf{I}-(\mathbf{K}_{12}^A\circ\mathbf{I})(\mathbf{K}_{22}^A\circ\mathbf{I}-\mathbf{K}_{22}^A)^{-1}(\mathbf{K}_{21}^A\circ\mathbf{I})\end{bmatrix}\begin{bmatrix}\mathbf{u}_1\\ \mathbf{u}_3\end{bmatrix}, \tag{59}$$

with the symmetry identity matrix

$$\mathbf{I}=\begin{bmatrix}1 & 1 & -1\\ -1 & -1 & 1\\ -1 & -1 & 1\end{bmatrix}. \tag{60}$$

The characteristic function for modal solutions is

$$\det\mathbf{K}=0. \tag{61}$$

For the calculation of the displacement and stress field components in a plate consisting of only one layer we abstain from using Rokhlin and Wang's backpropagation recursive algorithm, which is introduced below, and suggest to write Eq. (56) in the form

$$\begin{bmatrix}\boldsymbol{\sigma}_0^*\\ \boldsymbol{\sigma}_{-d}^*\end{bmatrix}=\begin{bmatrix}\mathbf{D}^- & \mathbf{D}^+\mathbf{H}\\ \mathbf{D}^-\mathbf{H} & \mathbf{D}^+\end{bmatrix}\begin{bmatrix}\mathbf{U}^-\\ \mathbf{U}^+\end{bmatrix}=\mathbf{D}\begin{bmatrix}\mathbf{U}^-\\ \mathbf{U}^+\end{bmatrix}=0 \tag{62}$$

instead, where $\mathbf{U}^-$ comprises the amplitudes of the three downward propagating partial waves U_i, $i=1,2,3$, and $\mathbf{U}^+$ contains the amplitudes of the three upward propagating ones U_j, $j=4,5,6$. The usual procedure is to set one partial wave amplitude as unity. Then one can determine the amplitudes of the other partial waves in terms of the first one. With setting $U_1=1$, our approach yields

$$\begin{bmatrix}U_2\\ U_3\\ U_4\\ U_5\\ U_6\end{bmatrix}=-\begin{bmatrix}d_{22} & d_{23} & d_{24} & d_{25} & d_{26}\\ d_{32} & d_{33} & d_{34} & d_{35} & d_{36}\\ d_{42} & d_{43} & d_{44} & d_{45} & d_{46}\\ d_{52} & d_{53} & d_{54} & d_{55} & d_{56}\\ d_{62} & d_{63} & d_{64} & d_{65} & d_{66}\end{bmatrix}^{-1}\begin{bmatrix}d_{21}\\ d_{31}\\ d_{41}\\ d_{51}\\ d_{61}\end{bmatrix}. \tag{63}$$

Now, the displacement and stress field components at any coordinate x_3 can be calculated according to Appendix E. To distinguish symmetric and antisymmetric modes, one must calculate u_1 for $x_3=0,d$. If both values have the same sign the mode is symmetric, and if they have the opposite sign the mode is antisymmetric.

The calculation of the displacements and stresses in a multilayered system is more sophisticated. According to Ref. 29, the displacement at the top and bottom of the system is given by

$$\mathbf{u}_0=\mathbf{P}_0^-\mathbf{U}_{\text{in}}+\mathbf{P}_0^+\mathbf{U}_{\text{r}},\quad \mathbf{u}_{-d}=\mathbf{P}_{-d}^-\mathbf{U}_{\text{t}}, \tag{64}$$

where $\mathbf{U}_{\text{in}}$, $\mathbf{U}_{\text{r}}$, and $\mathbf{U}_{\text{t}}$ are the incident, reflected, and transmitted waves at the top and bottom surfaces, respectively. However, instead of using the explicit relations for the stresses, as shown in Ref. 29, we suggest to use $\sigma_0^*,\sigma_{-d}^*=0$. Therefore, by substituting Eq. (64) into

$$\begin{bmatrix}\boldsymbol{\sigma}_0^*\\ \boldsymbol{\sigma}_{-d}^*\end{bmatrix}=\begin{bmatrix}\mathbf{K}_{11} & \mathbf{K}_{12}\\ \mathbf{K}_{21} & \mathbf{K}_{22}\end{bmatrix}\begin{bmatrix}\mathbf{u}_0\\ \mathbf{u}_{-d}\end{bmatrix}=0 \tag{65}$$

we obtain the simpler relation

$$\begin{bmatrix} \mathbf{U}_r \\ \mathbf{U}_t \end{bmatrix} = \begin{bmatrix} -\mathbf{K}_{11}\mathbf{P}_0^+ & -\mathbf{K}_{12}\mathbf{P}_{-d}^- \\ \mathbf{K}_{21}\mathbf{P}_0^+ & \mathbf{K}_{22}\mathbf{P}_{-d}^- \end{bmatrix}^{-1} \begin{bmatrix} \mathbf{K}_{11}\mathbf{P}_0^- \\ -\mathbf{K}_{21}\mathbf{P}_0^- \end{bmatrix} \mathbf{U}_{\text{in}}, \tag{66}$$

with

$$\mathbf{U}_{\text{in}} = \begin{bmatrix} 1 \\ 0 \\ 0 \end{bmatrix}. \tag{67}$$

Notice that $\mathbf{K}_{ij}$ are submatrices of the global stiffness matrix. With the now known reflection and transmission coefficients $\mathbf{U}_r$ and $\mathbf{U}_t$, Eq. (64) can be solved. In order to get the displacements and stresses at the inner interfaces, one should use the backpropagation recursive algorithm proposed by Rokhlin and Wang. In contrast to the procedure presented in Sec. II B 3, now one has to start with the lowermost layer m. The displacements at the bottom of this layer $\mathbf{u}_{-d}$ have already been obtained. Then, $\mathbf{u}_m$ at the top of this layer is given by

$$\mathbf{u}_m = (\mathbf{K}_{11}^m - \mathbf{K}_{22}^*)^{-1}\mathbf{K}_{21}^*\mathbf{u}_0 - (\mathbf{K}_{11}^m - \mathbf{K}_{22}^*)^{-1}\mathbf{K}_{12}^m\mathbf{u}_{m+1}, \tag{68}$$

where $\mathbf{K}^m$ is the local stiffness matrix of the mth layer and $\mathbf{K}^*$ is the total stiffness matrix of the top $m-1$ layers. This procedure has to be repeated until one has the displacements at the bottom of the top layer. Now, the six partial wave amplitudes for each layer can be calculated by

$$\begin{bmatrix} \mathbf{U}_m \\ \mathbf{U}_{m+1} \end{bmatrix} = \begin{bmatrix} \mathbf{P}^- & \mathbf{P}^+\mathbf{H} \\ \mathbf{P}^-\mathbf{H} & \mathbf{P}^+ \end{bmatrix}_m^{-1} \begin{bmatrix} \mathbf{u}_m \\ \mathbf{u}_{m+1} \end{bmatrix}. \tag{69}$$

Finally, Eqs. (E1) are used for each layer to get their respective displacement and stress field components inside the layers at the locations x'_3.

To distinguish between symmetric and antisymmetric modes in multilayered systems Eq. (64) is reduced to

$$u_1^0 = 1 + \begin{bmatrix} 1 \\ 1 \\ 1 \end{bmatrix} \mathbf{U}_r, \quad u_1^{-d} = \begin{bmatrix} 1 \\ 1 \\ 1 \end{bmatrix} \mathbf{U}_t. \tag{70}$$

B. Propagation along axes of symmetry

1. Lamb waves

In the case of decoupling between Lamb and shear horizontal modes, pure Lamb waves are formed through the superposition of only four partial waves, possessing displacement only along the x_1- and x_3-directions. Therefore, Eq. (5) reduces to

$$(u_1, u_3) = (U_1, U_3)\mathrm{e}^{\mathrm{i}k\alpha x'_3}, \tag{71}$$

wherein the common factor $\mathrm{e}^{\mathrm{i}k(x_1 - vt)}$ is suppressed. Substituting Eq. (71) into the expanded displacement field equations delivers

$$\begin{bmatrix} C_{11} - \rho v^2 + C_{55}\alpha^2 & (C_{13} + C_{55})\alpha \\ \text{sym} & C_{55} - \rho v^2 + C_{33}\alpha^2 \end{bmatrix} \begin{bmatrix} U_1 \\ U_3 \end{bmatrix} = 0. \tag{72}$$

Nontrivial solutions for U_1,U_3 require the vanishing of the determinant of the 2×2 matrix in Eq. (72) and yield the fourth-degree polynomial equation

$$A_1\alpha^4 + A_2\alpha^2 + A_3 = 0, \tag{73}$$

with the coefficients

$$\begin{aligned} A_1 &= C_{33}C_{55}, \\ A_2 &= C_{55}(C_{55} - \rho v^2) + C_{33}(C_{11} - \rho v^2) - (C_{13} + C_{55})^2, \\ A_3 &= (C_{55} - \rho v^2)(C_{11} - \rho v^2). \end{aligned} \tag{74}$$

Equation (73) admits four solutions α_q, $q = 1,2,\ldots,4$, according to

$$\alpha_q = \pm\sqrt{\frac{-A_2 \pm \sqrt{A_2^2 - 4A_1A_3}}{2A_1}}. \tag{75}$$

Substituting α_q into Eq. (72) delivers the partial wave amplitude ratio $W_q = U_{3q}/U_{1q}$, namely,

$$W_q = \frac{K_{11}(\alpha_q)}{K_{13}(\alpha_q)} = \frac{\rho v^2 - C_{11} - C_{55}\alpha_q^2}{(C_{13} + C_{55})\alpha_q}. \tag{76}$$

Now, the displacement and stress field components are represented as

$$\begin{aligned} (u_1, u_3) &= \sum_{q=1}^{4} (1, W_q) U_{1q} \mathrm{e}^{\mathrm{i}k\alpha x'_3}, \\ (\sigma_{33}^*\sigma_{13}^*) &= \sum_{q=1}^{4} (D_{1q}, D_{2q}) U_{1q} \mathrm{e}^{\mathrm{i}k\alpha x'_3}, \end{aligned} \tag{77}$$

with

$$D_{1q} = C_{13} + C_{33}\alpha_q W_q, \quad D_{2q} = C_{55}(\alpha_q + W_q). \tag{78}$$

Finally, the stiffness matrix in Eq. (D1) turns into Eq. (D2) as given in Appendix D 2. All further operations, which have been explained for the general layered case, can be conducted also in their reduced form in the decoupled case and need not be repeated here. It should only be noted that the symmetry identity matrix is now given as

$$\mathbf{I} = \begin{bmatrix} 1 & -1 \\ -1 & 1 \end{bmatrix}. \tag{79}$$

2. Shear horizontal waves

As stated in Sec. II B 1, antisymmetric shear horizontal modes could not have been computed in symmetric, multilayered systems in transfer matrix style. Instead, a relation

offered by Wang and Rokhlin[30] has been used, where the local stiffness matrix of the mth layer is given as

$$\mathbf{K}_m = \frac{\mathrm{i}C_{44}k_z}{e^2-1}\begin{bmatrix} -1-e^2 & 2e \\ -2e & 1+e^2 \end{bmatrix}, \tag{80}$$

where $e = \mathrm{e}^{\mathrm{i}k_z d_m}$ and $k_z = \sqrt{(\rho\omega^2 - C_{66}k^2)/C_{44}}$. Now, Eqs. (57)–(59) can be applied to obtain the global stiffness matrix (with the symmetry identity $I=-1$). However, in order to get the displacement and stress, one has to compute the individual local transfer matrices $\mathbf{A}_m^c$ according to Eq. (26). This can be done by entering the corresponding phase velocities, which have been obtained during the tracing procedure with the use of Eq. (80). Then one can apply Eqs. (42)–(55).

IV. DISPERSION CURVE TRACING

In the following, the tracing algorithms used by our Dispersion Calculator software are described. If higher order modes shall be traced, the program starts with a frequency sweep at a certain phase velocity, which is then the top phase velocity in the dispersion diagram (20 m/ms in Figs. 3 and 4). The cut-off frequencies of all occurring modes should be detected by that sweep. These modes are classified into four possible mode families (in case of the decoupling in a symmetric layup, one has symmetric and antisymmetric Lamb and shear horizontal waves). Then, three phase velocity sweeps are conducted after the symmetric and antisymmetric fundamental Lamb wave modes S_0, A_0, and the fundamental shear horizontal mode S'_0 at 1 Hz. The main condition is that the determinant has to be zero. In practice it will never be zero, so it is searched for a change in sign of the determinant between two increments. It is important to check also that the absolute value of the determinant is a minimum because there occur sign changes that are not accompanied by a minimum and do not indicate a modal solution. If a sign change that is also a minimum is detected between two increments, it is converged upon the root by three point bisection until the selected resolution is reached.

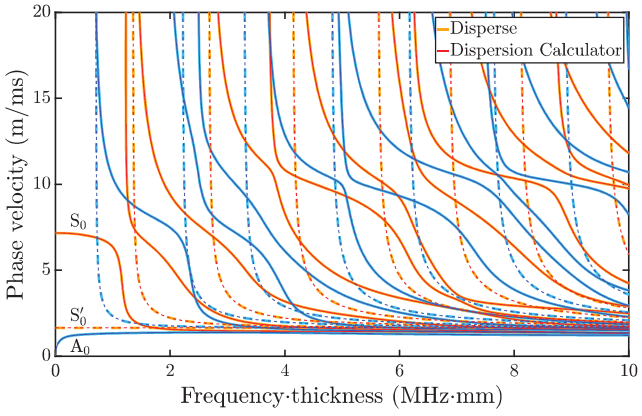

FIG. 3. Dispersion diagram for wave propagation along 0° in a 2 mm thick layup $[0/90]_{2s}$, T800/913. In this decoupled case one can distinguish between symmetric (red/orange) and antisymmetric (blue) Lamb- (solid lines) and shear horizontal waves (dashed lines). Notice that modes of the same family do not cross each other.

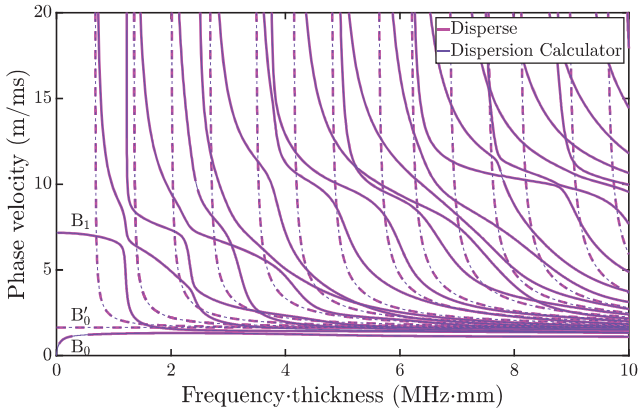

FIG. 4. Dispersion diagram for wave propagation along 0° in a 2 mm thick layup $[0/90]_4$, T800/913. Since Lamb and shear horizontal waves decouple, one can solve them separately, but because the layup is non-symmetric, the modes do not have a definite symmetric or antisymmetric character. Since we are not aware of an official notation for these non-symmetric modes, we denote them with the letter "B."

Each mode family has its own individual boundary conditions, which makes it possible to trace them separately (see Table I). In the decoupled case in symmetric layups, only modes belonging to different families cross each other (see Fig. 3), but since they have different boundary conditions, the well-known tracing problem of jumping to the wrong mode can be avoided completely. In the coupled case, in symmetric layups, it can be distinguished between two mode families, namely symmetric and antisymmetric modes (see Fig. 5). Now, crossing of modes belonging to the same family can occur and appropriate algorithms are required to control the jumping mode behavior in this case. The modes belonging to the same family are traced one after the other, starting with the fundamental mode and moving on in increasing mode order. This procedure is performed for every mode family, one after the other. Our program traces directly in the frequency space for the most part, i.e., the phase velocity is swept at certain frequency increments (usually between 1 and 10 kHz). Let us consider now the tracing

TABLE I. Boundary conditions used for the tracing of the six mode families.

Family	Situation	Boundary conditions
S		$\det\mathbf{K}=0,\ \ \mathrm{abs}(\det\mathbf{K})=\min,\ u_1^{++}$[a]
A		$\det\mathbf{K}=0,\ \ \mathrm{abs}(\det\mathbf{K})=\min,\ u_1^{+-}$[b]
B		$\det\mathbf{K}=0,\ \mathrm{abs}(\det\mathbf{K})=\min$
S'	Single layer	$a^r_{21(m)}=0$
	Single super layer	$\mathrm{abs}(a^r_{21})=\min$
	Periodic	$\mathrm{abs}\left(\det\begin{bmatrix} a^c_{11}-1 & a^c_{12} \\ a^c_{21} & a^c_{22}-1 \end{bmatrix}\right)=\min$
A'	Single layer	$a^r_{21(m)}=0$
	Else	$\det\mathbf{K}=0$
B'	Single super layer	$a^r_{21}=0$
	Per., $p/n=1,2,\ldots$Periodic	$a^r_{21}=0$
	Per., $p/n\neq 1,2,\ldots$	$\det\begin{bmatrix} a^c_{11}-1 & a^c_{12} \\ a^c_{21} & a^c_{22}+1 \end{bmatrix}=0$
S'_0, B'_0	Decoupled case	Non-dispersive, $v=\sqrt{C_{66}/\rho}$

[a] u_1 at the plate's top and bottom have the same sign.
[b] u_1 at the plate's top and bottom have the opposite sign.

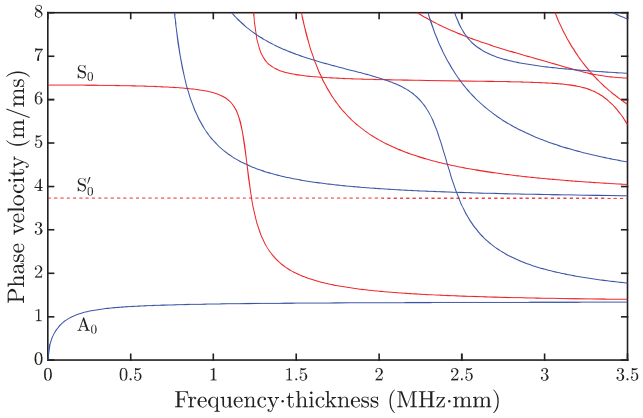

FIG. 5. Dispersion diagram for wave propagation along 0° in a 50 mm thick layup $[0/90/45/-45]_{50s}$, T800/913. Since the system is symmetric, one can determine symmetric and antisymmetric modes. Lamb and shear horizontal waves are coupled and the crossing of modes belonging to the same family occurs. The fundamental shear horizontal mode S'_0 can always be determined since it is located between S_0 and A_0. In contrast to its behavior in the decoupled case, S'_0 is now dispersive even though it can hardly be seen.

of the S_0 mode. By the initial phase velocity sweep, one has the phase velocity at 1 Hz. The second sample point, e.g., at 5 kHz (corresponding to 0.01 MHz mm, since the thickness is 2 mm), is expected to be at a lower phase velocity. Therefore, the phase velocity sweep starts from the phase velocity of the first sample point downward. For the tracing of all following sample points, the phase velocity interval, wherein the search is performed, reaches from just above the preceding sample point's phase velocity down by a certain multiple of the difference between the second to last and the last sample's phase velocity. The multiple is set to ten where dispersion curves have a negative curvature and two where they have a positive curvature like it is the case for the complete shear horizontal mode curves. In contrast to what was performed to find the first two samples, now the phase velocity interval is not divided into fixed increments initially. Instead, the bisection starts immediately unless a change of sign/minimum could not be found between the initial interval limits. This can happen if two modes are within the search interval (two sign changes are as if there was none), or simply if smaller increments have to be used in order to detect a root. In that case an n-loop, $n = 1,2,\ldots$, is initiated, wherein the interval is divided into 5^n increments, until a change of sign/minimum is detected. After that, the bisection of the two critical increments starts if the desired resolution has not already been achieved. This kind of prediction of the next sample point and adjustment of the search range accordingly is necessary in order to avoid extremely slow tracing and achieve small enough increments to be able to trace curves in some instances at all. The aforementioned multiple of ten ensures that samples are covered by the search interval, even if the curve's slope changes drastically, as is the case with S_0 and B_1 in Figs. 3–5 around 1 MHz mm (in this paper, the modes in non-symmetric layups are unconventionally denoted with the letter "B"). All modes tend to lower phase velocities with increasing frequency except A_0 and B_0. Sometimes, as is the case in Figs. 3 and 4, A_0 and B_0 have an apex. From then on the modes bend down and one must switch to the top-down routine like the one used for the other modes.

M. J. S. Lowe describes in Refs. 43 and 44 another tracing routine, which he utilizes in DISPERSE®. Here, an extrapolation method is used to make a guess for the next sample point. This works well in the wavenumber space since the curves are more straight there than in the frequency space.

If higher order modes are traced, the lower search interval limit is raised if necessary so that it just does not touch the next lower mode from the same mode family at the same frequency. In case of decoupling in symmetric layups it is clear that the currently traced mode does not go below the next lower mode anyway. However, in all other situations, the raising of the interval ensures that the tracing routine does not jump to a crossing mode of the same family that has already been traced. In this case, when a search is not successful above the lower mode because the current mode crosses that one, a new search interval is defined afterward, starting just below the lower mode to continue the tracing. This procedure is slow, but prevents the jumping to modes that have already been traced effectively. Of course though, before such an instance could happen, the lower mode must have crossed the higher mode before the latter one was traced. The jumping to yet unknown modes basically cannot be avoided in any case. If the jumping occurs, one has to try different tracing parameters like the frequency increments, for instance, to avoid it.

Higher order modes are also traced by phase velocity sweeps starting at their respective cut-off frequencies. However, since these modes are close to parallel to the phase velocity axis around their cut-off frequencies, the curves are often incomplete at high phase velocities. If this happens, frequency sweeps are performed to complete the curves to the upper phase velocity limit. M. J. S. Lowe offers one routing among others in DISPERSE®, where the sweeps are conducted normally to the dispersion curve's tangent. This prevents the aforementioned problem altogether.

As can be seen in Fig. 3, pure shear horizontal modes are special in that they never cross each other even if they belong to different families. Therefore, one can abstain from checking the polarity of the displacement u_2 at the plate's top and bottom during the tracing. This is only done to classify the modes in the course of the initial frequency sweep. Furthermore, the curve tracings of both families are already distinguished through the use of different functions, except if the plate is single layered.

V. NUMERICAL EXAMPLES

In this section we present our calculations on the fiber-matrix system T800/913 by using our Dispersion Calculator software. The density of T800/913 of 1550 kg/m^3 and the stiffness matrix (in GPa) were taken from Ref. 46,

$$C'_{\mathrm{T800/913}} = \begin{bmatrix} 154 & 3.7 & 3.7 & 0 & 0 & 0 \\ & 9.5 & 5.2 & 0 & 0 & 0 \\ & & 9.5 & 0 & 0 & 0 \\ & & & 2.15 & 0 & 0 \\ & & \mathrm{sym} & & 4.2 & 0 \\ & & & & & 4.2 \end{bmatrix}. \quad (81)$$

First, we demonstrate the calculation of the different mode families on 2 mm thick $[0/90]_{2s}$ and $[0/90]_4$ layups. The corresponding dispersion curves are compared to those obtained with DISPERSE®. Then we compute 50 mm thick $[0/90/45/-45]_{10s}$ and $[0/90/45/-45]_{50s}$ layups in order to prove the capabilities of our method on laminates with large numbers of layers. These laminates cannot be calculated with DISPERSE® currently. For consistency, the wave propagation is always along 0°.

A. Dispersion diagrams

Figure 3 displays the dispersion diagram for wave propagation along 0° in the 2 mm thick layup $[0/90]_{2s}$. Lamb and shear horizontal modes are decoupled and have a definite symmetric or antisymmetric character. The bold curves are calculated by DISPERSE® and the thin curves by the Dispersion Calculator. Clearly, the curves of both softwares are matching regarding the shape as well as the mode type. In Table II we give the average and maximum deviation of the sample points of S_0 and S_2 calculated by the Dispersion Calculator from the ones obtained by DISPERSE®. The frequency step in the dispersion curves is 1 kHz, i.e., S_0 consists of 5000 samples. Figure 4 shows the dispersion diagram for wave propagation along 0° in the 2 mm thick layup $[0/90]_4$. Due to the non-symmetric layup, the modes do not have a definite symmetric or antisymmetric shape. Hence, the solutions can be separated only into shear horizontal- and Lamb wave modes. Again, our results match those of DISPERSE®. It was already said that modern rocket booster pressure vessels can consist of up to 400 layers in certain areas and it is the main requisite that the Dispersion Calculator must be able to calculate such laminates since rocket booster layups are of such complexity that no grouping of layers can be applied. We assume a layup $[0/90/45/-45]_{50s}$ with layer thicknesses of 0.125 mm yielding a 50 mm thick laminate. The dispersion diagram is presented in Fig. 5. The calculation of that diagram took 101 min on an i7–2700 K central processing unit (CPU) at 4×3.5 GHz (Intel, Santa Clara, CA). The processing time is strongly dependent on the curve tracing algorithms, most importantly on the as precise as possible prediction of the next sample point's phase velocity. This can be taken care of by optimal tracing parameters available in the software. Finally, we study the effect of the grouping of layers on the dispersion diagrams. Therefore, the prior layup is approximated by $[0/90/45/-45]_{10s}$ with layer thicknesses of 0.625 mm, having only 80 layers. This calculation took 15 min. The dispersion curves are compared in Fig. 6. Whereas the fundamental modes S_0 and A_0 are matching very well, there are notable differences in the higher order modes. Therefore, the approximative calculation is suitable for applications like the non-destructive testing, where one is interested in A_0 for the most part, but not for an in-depth modal analysis.

TABLE II. Deviation of the Dispersion Calculator from DISPERSE® in Fig. 3.

	S_0	S_2
Average deviation (m/ms)	2.08×10^{-5}	1.13×10^{-4}
Average deviation (%)	4.55×10^{-4}	8.23×10^{-4}
Maximum deviation (m/ms)	1.30×10^{-3}	2.58×10^{-2}
Maximum deviation (%)	2.00×10^{-2}	1.37×10^{-1}

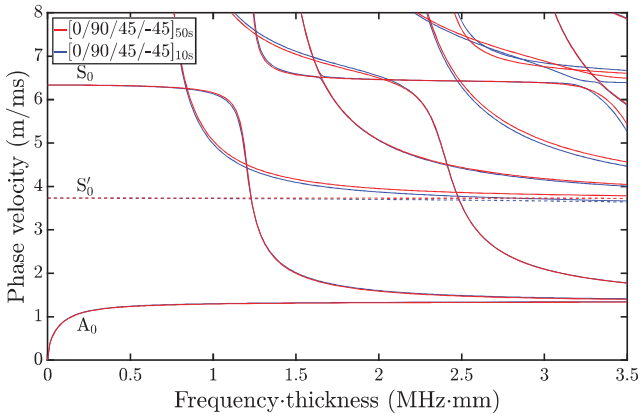

FIG. 6. Comparison of 50 mm thick layups $[0/90/45/-45]_{50s}$ and $[0/90/45/-45]_{10s}$, T800/913. While S_0 and A_0 are matching well, there are differences in the higher order modes.

B. Displacement and stress profiles

In Fig. 7, the displacement and stress field components are displayed for three exemplary modes at certain frequencies. Since these components have been calculated with respect to one arbitrarily chosen partial wave amplitude, absolute numbers have no physical meaning. However, these profiles represent the correct ratios between the three components. Since the field components are complex numbers, one has to establish a certain convention about which component should be analyzed. The left-hand diagrams display the relative displacements real(u_1), real(u_2), and imag(u_3) and the right-hand diagrams display the relative stresses real(σ_{33}), imag(σ_{13}), and imag(σ_{23}). This choice has been made in order to be able to compare with DISPERSE®.

Figure 7(a) shows the displacements versus the plate thickness for S_0 at 2 MHz as appears in Fig. 3. Since Lamb and shear horizontal modes are decoupled, it is a pure Lamb wave, so the u_2-component is zero. As the u_1-components at the top and bottom have the same sign, this mode is identified to be symmetric. Figure 7(b) displays the corresponding stresses. According to the free wave condition, all components are zero at the plate's surfaces. In this picture, one can distinguish eight sections in the profiles very well, which correspond to the eight layers in $[0/90]_{2s}$. Figures 7(c) and 7(d) depict the displacement and stress, respectively, of the pure shear horizontal mode A_3' from the same dispersion diagram in Fig. 3. Only the u_2- and σ_{23}-component are non-zero and the shape of u_2 determines this mode's character to be antisymmetric. Interestingly enough, the shape of both profiles is independent of the frequency, unlike the case in Lamb waves. In Figs. 7(e) and 7(f), A_2 is analyzed at 70 kHz in $[0/90/45/-45]_{50s}$ from Fig. 5. Since there are 45°-layers in the layup, the mode is coupled and all six displacement and stress field components are non-zero. Again, the antisymmetric character is indicated by u_1 at the top and bottom of the

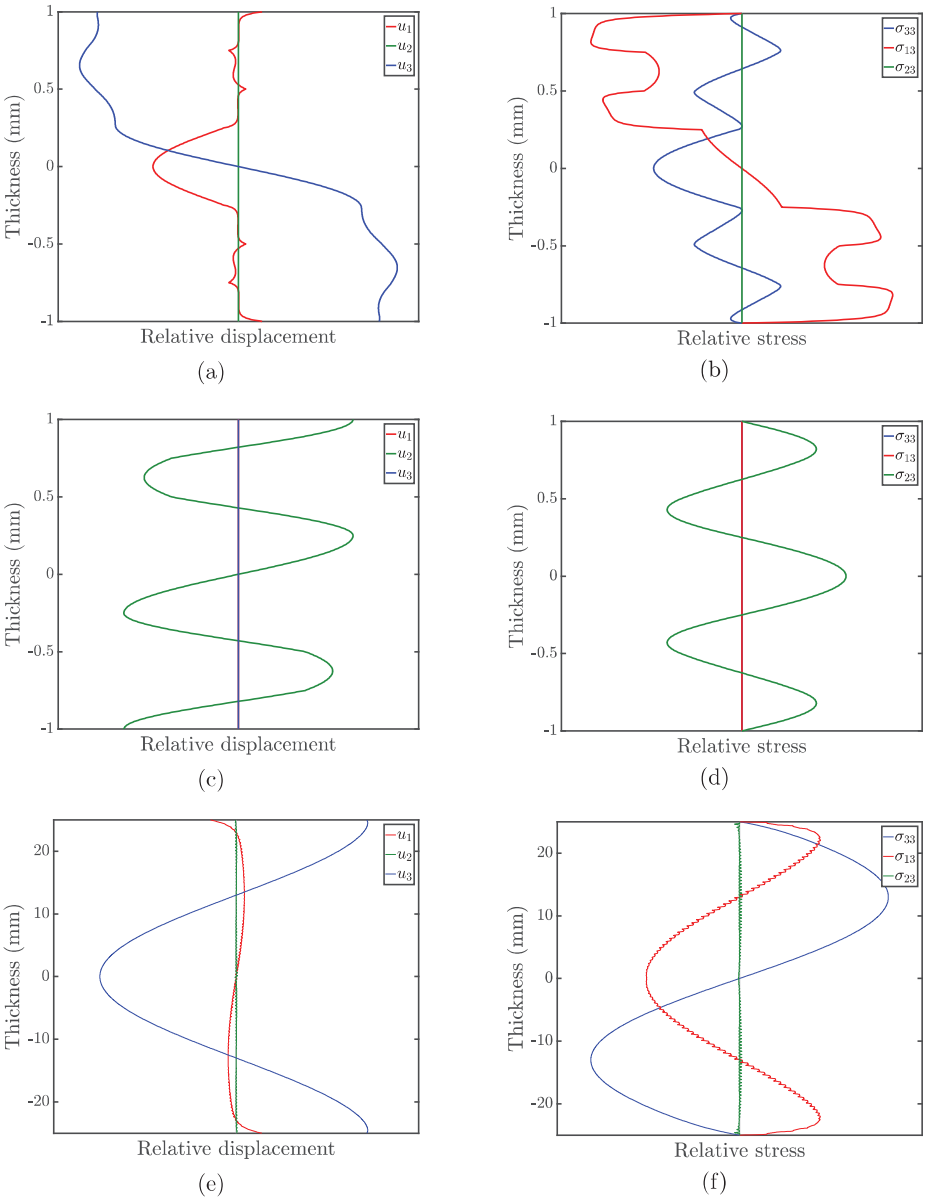

FIG. 7. The left-hand diagrams show the relative displacements (real or imaginary part), real(u_1), real(u_2). and imag(u_3), and the right-hand diagrams show the relative stresses real(σ_{33}), imag(σ_{13}), and imag(σ_{23}) for selected modes versus the plate thickness. (a),(b) S_0 at 2 MHz in $[0/90]_{2s}$. (c),(d) A'_3 in $[0/90]_{2s}$. (e),(f) A_2 at 70 kHz in $[0/90/45/-45]_{50s}$.

plate. The periodicity of the layup becomes obvious in the displacements u_1 and u_2 and the shear stresses σ_{13} and σ_{23}.

It provides an interesting insight into a Lamb wave, if one animates the mode shape through the reintroduction of the factor $e^{ik(x_1-vt)}$. Figure 8 shows one frame in such a calculation of the B_3 mode at 3 MHz in the non-symmetric layup $[0/90]_4$ (see Fig. 4), where the wave propagation is along 0°. It is important to keep in mind that, unlike the case in symmetric layups, u_1 at the top and bottom can change sign with frequency, so that it is impossible to determine a definite symmetric or antisymmetric character.

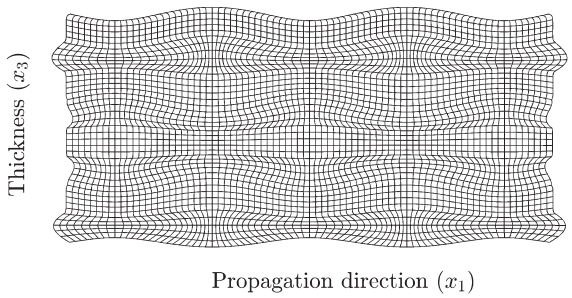

FIG. 8. Mode shape of B_3 at 3 MHz in a 2 mm thick layup $[0/90]_4$, T800/913.

VI. CONCLUSIONS

It was shown that laminates consisting of up to 400 layers can be calculated by using the stiffness matrix method. In this aspect it is superior to DISPERSE®, which currently cannot calculate laminates containing more than 64 layers. By the classification of the modal solutions into the different mode families, the robustness and retrieved information about the modes obtained by the stiffness matrix method was significantly improved. Validation of the program was made against the DISPERSE® results for $[0/90]_{2s}$ and $[0/90]_4$ thin laminates, which showed remarkable 99.9994% agreement. With a typical computer it is now

possible to calculate dispersion curves for thick walled laminates. The program will be made available as freeware on the DLR homepage.[28]

ACKNOWLEDGMENTS

The authors would like to thank Professor Michael J. S. Lowe for his sound advice and valuable time spent on discussions that helped to carry out the implementation of the stiffness matrix method successfully, as well as for his suggestions on the paper itself. The authors gratefully acknowledge support from the Free State of Bavaria under research Grant No. LABAY88.

APPENDIX A: TRANSFORMED STIFFNESS MATRIX COMPONENTS

$$
\begin{aligned}
C_{11} &= C'_{11}\cos^4\Phi + C'_{22}\sin^4\Phi + 2(C'_{12}+2C'_{66})\sin^2\Phi\cos^2\Phi,\\
C_{13} &= C'_{13}\cos^2\Phi + C'_{23}\sin^2\Phi,\\
C_{16} &= (C'_{12}+2C'_{66}-C'_{11})\sin\Phi\cos^3\Phi + (C'_{22}-C'_{12}-2C'_{66})\cos\Phi\sin^3\Phi,\\
C_{33} &= C'_{33},\\
C_{36} &= (C'_{23}-C'_{13})\sin\Phi\cos\Phi,\\
C_{44} &= C'_{44}\cos^2\Phi + C'_{55}\sin^2\Phi,\\
C_{45} &= (C'_{44}-C'_{55})\sin\Phi\cos\Phi,\\
C_{55} &= C'_{55}\cos^2\Phi + C'_{55}\sin^2\Phi,\\
C_{66} &= C'_{66} + (C'_{11}+C'_{22}-2C'_{12}-4C'_{66})\sin^2\Phi\cos^2\Phi.
\end{aligned}
\tag{A1}
$$

APPENDIX B: POLYNOMIAL COEFFICIENTS

$$
\begin{aligned}
A_1 &= \big[2(C_{13}C_{36}C_{45} - C_{16}C_{33}C_{45} - C_{13}C_{44}C_{55} + C_{13}C_{45}^2) + C_{11}C_{33}C_{44} + C_{33}C_{55}C_{66} - C_{44}C_{13}^2 - C_{55}C_{36}^2\\
&\quad - (C_{33}C_{44} + C_{33}C_{55} + C_{44}C_{55} - C_{45}^2)\rho v^2\big]/\Delta,\\
A_2 &= \big[2(C_{13}C_{16}C_{36} + C_{13}C_{16}C_{45} + C_{16}C_{36}C_{55} - C_{13}C_{55}C_{66} - C_{11}C_{36}C_{45}) + C_{11}C_{33}C_{66} + C_{11}C_{44}C_{55} - C_{11}C_{36}^2\\
&\quad - C_{33}C_{16}^2 - C_{11}C_{45}^2 - C_{66}C_{13}^2 + (2(C_{16}C_{45} + C_{13}C_{55} + C_{36}C_{45}) - C_{11}C_{33} - C_{11}C_{44} - C_{33}C_{66} - C_{44}C_{55}\\
&\quad - C_{55}C_{66} + C_{13}^2 + C_{36}^2 + C_{45}^2)\rho v^2 + (C_{33} + C_{44} + C_{55})\rho^2 v^4\big]/\Delta,\\
A_3 &= \big[C_{11}C_{55}C_{66} - C_{55}C_{16}^2 - (C_{11}C_{55} + C_{11}C_{66} + C_{55}C_{66} - C_{16}^2)\rho v^2 + (C_{11} + C_{55} + C_{66})\rho^2 v^4 - \rho^3 v^6\big]/\Delta
\end{aligned}
\tag{B1}
$$

with

$$
\Delta = C_{33}C_{44}C_{55} - C_{33}C_{45}^2. \tag{B2}
$$

APPENDIX C: EXPANDED MATRIX FORM OF THE TRANSFER MATRIX METHOD

$$
\begin{bmatrix} u_1\\ u_2\\ u_3\\ \sigma^*_{33}\\ \sigma^*_{13}\\ \sigma^*_{23}\end{bmatrix} =
\begin{bmatrix}
1 & 1 & 1 & 1 & 1 & 1\\
V_1 & V_1 & V_3 & V_3 & V_5 & V_5\\
W_1 & -W_1 & W_3 & -W_3 & W_5 & -W_5\\
D_{11} & D_{11} & D_{13} & D_{13} & D_{15} & D_{15}\\
D_{21} & -D_{21} & D_{23} & -D_{23} & D_{25} & -D_{25}\\
D_{31} & -D_{31} & D_{33} & -D_{33} & D_{35} & -D_{35}
\end{bmatrix}
\cdot
\begin{bmatrix}
e^{ik\alpha_1 x'_3} & 0 & 0 & 0 & 0 & 0\\
0 & e^{ik\alpha_2 x'_3} & 0 & 0 & 0 & 0\\
0 & 0 & e^{ik\alpha_3 x'_3} & 0 & 0 & 0\\
0 & 0 & 0 & e^{ik\alpha_4 x'_3} & 0 & 0\\
0 & 0 & 0 & 0 & e^{ik\alpha_5 x'_3} & 0\\
0 & 0 & 0 & 0 & 0 & e^{ik\alpha_6 x'_3}
\end{bmatrix}
\begin{bmatrix} U_{11}e^{ik(x_1-vt)}\\ U_{12}e^{ik(x_1-vt)}\\ U_{13}e^{ik(x_1-vt)}\\ U_{14}e^{ik(x_1-vt)}\\ U_{15}e^{ik(x_1-vt)}\\ U_{16}e^{ik(x_1-vt)}\end{bmatrix}.
\tag{C1}
$$

APPENDIX D: EXPANDED MATRIX FORMS OF THE STIFFNESS MATRIX METHOD

1. General layered composite

$$\begin{bmatrix} \sigma_{33}^{*m} \\ \sigma_{13}^{*m} \\ \sigma_{23}^{*m} \\ \sigma_{33}^{*m+1} \\ \sigma_{13}^{*m+1} \\ \sigma_{23}^{*m+1} \end{bmatrix} = \begin{bmatrix} D_{11} & D_{13} & D_{15} & D_{11}e^{ik\alpha_1 d_m} & D_{13}e^{ik\alpha_3 d_m} & D_{15}e^{ik\alpha_5 d_m} \\ D_{21} & D_{23} & D_{25} & -D_{21}e^{ik\alpha_1 d_m} & -D_{23}e^{ik\alpha_3 d_m} & -D_{25}e^{ik\alpha_5 d_m} \\ D_{31} & D_{33} & D_{35} & -D_{31}e^{ik\alpha_1 d_m} & -D_{33}e^{ik\alpha_3 d_m} & -D_{35}e^{ik\alpha_5 d_m} \\ D_{11}e^{ik\alpha_1 d_m} & D_{13}e^{ik\alpha_3 d_m} & D_{15}e^{ik\alpha_5 d_m} & D_{11} & D_{13} & D_{15} \\ D_{21}e^{ik\alpha_1 d_m} & D_{23}e^{ik\alpha_3 d_m} & D_{25}e^{ik\alpha_5 d_m} & -D_{21} & -D_{23} & -D_{25} \\ D_{31}e^{ik\alpha_1 d_m} & D_{33}e^{ik\alpha_3 d_m} & D_{35}e^{ik\alpha_5 d_m} & -D_{31} & -D_{33} & -D_{35} \end{bmatrix}$$

$$\times \begin{bmatrix} 1 & 1 & 1 & e^{ik\alpha_1 d_m} & e^{ik\alpha_3 d_m} & e^{ik\alpha_5 d_m} \\ V_1 & V_3 & V_5 & V_1 e^{ik\alpha_1 d_m} & V_3 e^{ik\alpha_3 d_m} & V_5 e^{ik\alpha_5 d_m} \\ W_1 & W_3 & W_5 & -W_1 e^{ik\alpha_1 d_m} & -W_3 e^{ik\alpha_3 d_m} & -W_5 e^{ik\alpha_5 d_m} \\ e^{ik\alpha_1 d_m} & e^{ik\alpha_3 d_m} & e^{ik\alpha_5 d_m} & 1 & 1 & 1 \\ V_1 e^{ik\alpha_1 d_m} & V_3 e^{ik\alpha_3 d_m} & V_5 e^{ik\alpha_5 d_m} & V_1 & V_3 & V_5 \\ W_1 e^{ik\alpha_1 d_m} & W_3 e^{ik\alpha_3 d_m} & W_5 e^{ik\alpha_5 d_m} & -W_1 & -W_3 & -W_5 \end{bmatrix}^{-1} \begin{bmatrix} u_1^m \\ u_2^m \\ u_3^m \\ u_1^{m+1} \\ u_2^{m+1} \\ u_3^{m+1} \end{bmatrix}. \tag{D1}$$

2. Propagation along axes of symmetry

$$\begin{bmatrix} \sigma_{33}^{*m} \\ \sigma_{13}^{*m} \\ \sigma_{33}^{*m+1} \\ \sigma_{13}^{*m+1} \end{bmatrix} = \begin{bmatrix} D_{11} & D_{13} & D_{11}e^{ik\alpha_1 d_m} & D_{13}e^{ik\alpha_3 d_m} \\ D_{21} & D_{23} & -D_{21}e^{ik\alpha_1 d_m} & -D_{23}e^{ik\alpha_3 d_m} \\ D_{11}e^{ik\alpha_1 d_m} & D_{13}e^{ik\alpha_3 d_m} & D_{11} & D_{13} \\ D_{21}e^{ik\alpha_1 d_m} & D_{23}e^{ik\alpha_3 d_m} & -D_{21} & -D_{23} \end{bmatrix}$$

$$\times \begin{bmatrix} 1 & 1 & e^{ik\alpha_1 d_m} & e^{ik\alpha_3 d_m} \\ W_1 & W_3 & -W_1 e^{ik\alpha_1 d_m} & -W_3 e^{ik\alpha_3 d_m} \\ e^{ik\alpha_1 d_m} & e^{ik\alpha_3 d_m} & 1 & 1 \\ W_1 e^{ik\alpha_1 d_m} & W_3 e^{ik\alpha_3 d_m} & -W_1 & -W_3 \end{bmatrix}^{-1} \begin{bmatrix} u_1^m \\ u_3^m \\ u_1^{m+1} \\ u_3^{m+1} \end{bmatrix}. \tag{D2}$$

APPENDIX E: DISPLACEMENT AND STRESS FIELD COMPONENTS

$$\begin{aligned} u_1 &= U_1 e^{ik\alpha_1 x_3} + U_2 e^{ik\alpha_3 x_3} + U_3 e^{ik\alpha_5 x_3} + U_4 e^{ik\alpha_1 (d-x_3)} + U_5 e^{ik\alpha_3 (d-x_3)} + U_6 e^{ik\alpha_5 (d-x_3)}, \\ u_2 &= V_1 U_1 e^{ik\alpha_1 x_3} + V_3 U_2 e^{ik\alpha_3 x_3} + V_5 U_3 e^{ik\alpha_5 x_3} + V_1 U_4 e^{ik\alpha_1 (d-x_3)} + V_3 U_5 e^{ik\alpha_3 (d-x_3)} + V_5 U_6 e^{ik\alpha_5 (d-x_3)}, \\ u_3 &= W_1 U_1 e^{ik\alpha_1 x_3} + W_3 U_2 e^{ik\alpha_3 x_3} + W_5 U_3 e^{ik\alpha_5 x_3} - W_1 U_4 e^{ik\alpha_1 (d-x_3)} - W_3 U_5 e^{ik\alpha_3 (d-x_3)} - W_5 U_6 e^{ik\alpha_5 (d-x_3)}, \\ \sigma_{33}^* &= D_{11} U_1 e^{ik\alpha_1 x_3} + D_{13} U_2 e^{ik\alpha_3 x_3} + D_{15} U_3 e^{ik\alpha_5 x_3} + D_{11} U_4 e^{ik\alpha_1 (d-x_3)} + D_{13} U_5 e^{ik\alpha_3 (d-x_3)} + D_{15} U_6 e^{ik\alpha_5 (d-x_3)}, \\ \sigma_{13}^* &= D_{21} U_1 e^{ik\alpha_1 x_3} + D_{23} U_2 e^{ik\alpha_3 x_3} + D_{25} U_3 e^{ik\alpha_5 x_3} - D_{21} U_4 e^{ik\alpha_1 (d-x_3)} - D_{23} U_5 e^{ik\alpha_3 (d-x_3)} - D_{25} U_6 e^{ik\alpha_5 (d-x_3)}, \\ \sigma_{23}^* &= D_{31} U_1 e^{ik\alpha_1 x_3} + D_{33} U_2 e^{ik\alpha_3 x_3} + D_{35} U_3 e^{ik\alpha_5 x_3} - D_{31} U_4 e^{ik\alpha_1 (d-x_3)} - D_{33} U_5 e^{ik\alpha_3 (d-x_3)} - D_{35} U_6 e^{ik\alpha_5 (d-x_3)}. \end{aligned} \tag{E1}$$

[1]I. Viktorov, *Rayleigh and Lamb Waves: Physical Theory and Applications* (Plenum, New York, 1967), pp. 123–144.
[2]M. Luukkala, P. Heikkila, and J. Surakka, "Plate wave resonance—A contactless test method," Ultrasonics **9**(4), 201–208 (1971).
[3]M. Luukkala and P. Meriläinen, "Metal plate testing using airborne ultrasound," Ultrasonics **11**(5), 218–221 (1973).
[4]P. D. Wilcox, M. J. S. Lowe, and P. Cawley, "Mode and transducer selection for long range Lamb wave inspection," J. Intell. Mater. Syst. Struct. **12**, 553–565 (2001).
[5]M. J. S. Lowe, D. N. Alleyne, and P. Cawley, "Defect detection in pipes using guided waves," Ultrasonics **36**, 147–154 (1998).
[6]M. J. S. Lowe and P. Cawley, "The applicability of plate wave techniques for the inspection of adhesive and diffusion bonded joints," J. Nondestr. Eval. **13**(4), 185–200 (1994).
[7]T. Kundu, A. Maji, T. Gosh, and K. Maslov, "Detection of kissing bonds by Lamb waves," Ultrasonics **35**, 573–580 (1998).
[8]K. Maslov and T. Kundu, "Selection of Lamb modes for detecting internal defects in composite laminates," Ultrasonics **35**, 141–150 (1997).
[9]S. S. Kessler, S. M. Spearing, and C. Soutis, "Damage detection in composite materials using Lamb wave methods," Smart Mater. Struct. **11**, 269–278 (2002).
[10]N. Toyama, J. Noda, and T. Okabe, "Quantitative damage detection in cross-ply laminates using Lamb wave method," Compos. Sci. Technol. **63**, 1473–1479 (2003).
[11]Z. Su, L. Ye, and Y. Lu, "Guided Lamb waves for identification of damage in composite structures: A review," J. Sound Vib. **295**, 753–780 (2006).
[12]K. Diamanti and C. Soutis, "Structural health monitoring techniques for aircraft composite structures," Prog. Aeronaut. Sci. **46**, 342–352 (2010).
[13]A. S. Purekar and D. J. Pines, "Damage detection in thin composite laminates using piezoelectric phased sensor arrays and guided Lamb wave interrogation," J. Intell. Mater. Syst. Struct. **21**, 995–1010 (2010).
[14]C. Ramadas, K. Balasubramaniam, M. Joshi, and C. V. Krishnamurthy, "Sizing of interface delamination in a composite T-joint using time-of-flight of Lamb waves," J. Intell. Mater. Syst. Struct. **22**, 757–768 (2011).
[15]H. Cunfu, L. Hongye, L. Zenghua, and W. Bin, "The propagation of coupled Lamb waves in multilayered arbitrary anisotropic composite laminates," J. Sound Vib. **332**, 7243–7256 (2013).
[16]M. Castaings and P. Cawley, "The generation, propagation, and detection of Lamb waves in plates using air-coupled ultrasonic transducers," J. Acoust. Soc. Am. **100**(5), 3070–3077 (1996).
[17]M. Castaings, P. Cawley, R. Farlow, and G. Hayward, "Single sided inspection of composite materials using air coupled ultrasound," J. Nondestr. Eval. **17**(1), 37–45 (1998).
[18]M. Castaings and B. Hosten, "Lamb and SH waves generated and detected by air-coupled ultrasonic transducers in composite material plates," NDT&E Int. **34**, 249–258 (2001).
[19]M. Castaings and B. Hosten, "Ultrasonic guided waves for health monitoring of high-pressure composite tanks," NDT&E Int. **41**, 648–655 (2008).
[20]I. Solodov, R. Stoessel, and G. Busse, "Material characterization and NDE using focused slanted transmission mode of air-coupled ultrasound," Res. Nondestr. Eval. **15**(2), 65–85 (2004).
[21]I. Solodov, K. Pfleiderer, H. Gerhard, and G. Busse, "Nonlinear acoustic approach to material characterisation of polymers and composites in tensile tests," Ultrasonics **42**, 1011–1015 (2004).
[22]I. Solodov, K. Pfleiderer, H. Gerhard, S. Predak, and G. Busse, "New opportunities for NDE with air-coupled ultrasound," NDT&E Int. **39**(3), 176–183 (2006).
[23]M. Rheinfurth, F. Schmidt, D. Döring, I. Solodov, G. Busse, and P. Horst, "Air-coupled guided waves combined with thermography for monitoring fatigue in biaxially loaded composite tubes," Compos. Sci. Technol. **71**(5), 600–608 (2011).
[24]M. Rheinfurth, N. Kosmann, D. Sauer, G. Busse, and K. Schulte, "Lamb waves for non-contact fatigue state evaluation of composites under various mechanical loading conditions," Composites: Part A **43**, 1203–1211 (2012).
[25]S. D. Holland and D. E. Chimenti, "High contrast air-coupled acoustic imaging with zero group velocity Lamb modes," Ultrasonics **42**, 957–960 (2004).
[26]R. Raisutis, R. Kazys, E. Zukauskas, and L. Mazeika, "Ultrasonic air-coupled testing of square-shape CFRP composite rods by means of guided waves," NDT&E Int. **44**, 645–654 (2011).
[27]L. Zenghua, Y. Hongtao, H. Cunfu, and W. Bin, "Delamination damage detection of laminated composite beams using air-coupled ultrasonic transducers," Sci. China: Phys., Mech. Astron. **56**(7), 1269–1279 (2013).
[28]Dispersion Calculator Rev. 1.0, available at https://www.dlr.de/bt/en/desktopdefault.aspx/tabid-2478/11208_read-53373/ (Last viewed 4 December 2018).
[29]S. I. Rokhlin and L. Wang, "Stable recursive algorithm for elastic wave propagation in layered anisotropic media: Stiffness matrix method," J. Acoust. Soc. Am. **112**(3), 822–834 (2002).
[30]L. Wang and S. I. Rokhlin, "Stable reformulation of transfer matrix method for wave propagation in layered anisotropic media," Ultrasonics **39**, 413–424 (2001).
[31]W. T. Thomson, "Transmission of elastic waves through as stratified solid medium," J. Appl. Phys. **21**, 89–93 (1950).
[32]N. A. Haskell, "The dispersion of surface waves on multilayered media," Bull. Seism. Soc. Am. **43**(1), 17–34 (1953).
[33]A. H. Nayfeh, *Wave Propagation in Layered Anisotropic Media with Applications to Composites* (North-Holland, Amsterdam, 1995), pp. 1–152.
[34]L. Knopoff, "A matrix method for elastic wave problems," Bull. Seism. Soc. Am. **54**(1), 431–438 (1964).
[35]H. Schmidt and G. Tango, "Efficient global matrix approach to the computation of synthetic seismograms," Geophys. J. R. Astr. Soc. **84**, 331–359 (1986).
[36]A. K. Mal, "Wave propagation in layered composite laminates under periodic surface loads," Wave Motion **10**(3), 257–266 (1988).
[37]E. Kausel and J. M. Roesset, "Stiffness matrices for layered soils," Bull. Seis. Soc. Am. **71**(6), 1743–1761 (1981).
[38]V. G. A. Kamal and V. Giurgiutiu, "Stiffness transfer matrix method (STMM) for stable dispersion curves solution in anisotropic composites," Proc. SPIE **9064** (2014).
[39]M. Barski and P. Pajak, "Determination of dispersion curves for composite materials with the use of stiffness matrix method," Acta Mech. Autom. **11**(2), 121–128 (2017).
[40]L. Gavric, "Computation and propagative waves in free rail using a finite element technique," J. Sound Vib. **185**(3), 531–543 (1995).
[41]F. H. Quintanilla, M. J. S. Lowe, and R. V. Craster, "Modeling guided elastic waves in generally anisotropic media using a spectral collocation method," J. Acoust. Soc. Am. **137**(3), 1180–1194 (2015).
[42]F. H. Quintanilla, M. J. S. Lowe, and R. V. Craster, "The symmetry and coupling properties of solutions in general anisotropic multilayer waveguides," J. Acoust. Soc. Am. **141**(1), 406–418 (2017).
[43]M. Lowe and B. Pavlakovic, *Disperse User's Manual* (Imperial College London, London, 2013), pp. 1–207.
[44]M. J. S. Lowe, "Matrix techniques for modeling ultrasonic waves in multilayered media," IEEE Trans. Ultrason., Ferroelect., Freq. Control **42**(4), 525–542 (1995).
[45]B. A. Auld, *Acoustic Fields and Waves in Solids*, 2nd ed. (Krieger, Malabar, FL, 1990), p. 165.
[46]M. Sause and M. Hamstad, *Acoustic Emission Analysis* (Academic, Oxford, 2018), p. 300.